

CO₂ Photoactivation Study of Adenine Nucleobase: Role of Hydrogen-Bonding Traction

Ning Li, Su-Juan Yao, Mei-Jie Wei, Jun He,* Weijie Chi,* and Ya-Qian Lan*

The discovery and in-depth study of non-biocatalytic applications of active biomolecules are essential for the development of biomimicry. Here, the effect of intermolecular hydrogen-bonding traction on the CO₂ photoactivation performance of adenine nucleobase by means of an adenine-containing model system (AMOF-1–4) is uncovered. Remarkably, the hydrogen-bonding schemes around adenines are regularly altered with the increase in the alkyl (methyl, ethyl, isopropyl, and *tert*-butyl) electron-donating capacity of the coordinated aliphatic carboxylic acids, and thus, lead to a stepwise improvement in CO₂ photoreduction activity. Density functional theory calculations demonstrate that strong intermolecular hydrogen-bonding traction surrounding adenine can obviously increase the adenine-CO₂ interaction energy and, therefore, result in a smoother CO₂ activation process. Significantly, this work also provides new inspiration for expanding the application of adenine to more small-molecule catalytic reactions.

be explored but catalytic reactions can also be performed in a green, inexpensive, and sustainable manner.^[2] However, the specific and complex living environment in which most biomolecules are located is usually difficult to simulate, and therefore, the artificial biomimetic catalysis generated by limited cognition is still not comparable to enzymatic catalysis.^[3] In this context, exploring the non-biocatalytic potentials of biomolecules implies an even more daunting task, as it often requires a lot of trial and error and even serendipities.

Adenine, being a purine nucleobase with an exocyclic amino group and four imino nitrogens, is an important naturally occurring active biomolecule found in nucleic acids. With the amino group and multiple imino nitrogens, adenine

1. Introduction

Studying the catalytic role of active biomolecules in living organisms has always been extremely important for a deep understanding of biochemical processes and the development of possible artificial biomimetic catalytic reactions.^[1] Moreover, if such active biomolecules are used directly as catalytic centers for artificially manipulated abiotic catalytic reactions, not only can their new potential applications outside of living organisms

molecules can form stable hydrogen-bonding schemes (e.g., double-helical DNA) or metal-nucleobase coordination backbones in living bodies.^[4] This allows adenine units to play crucial roles in certain biocatalytic reactions (e.g., catalysis in group II intron and at the ribosomal peptidyltransferase center) and biochemical processes (as an inextricable part of enzyme cofactors and second messenger systems).^[5] Moreover, based on strong hydrogen-bonding capacity and versatile coordination with metal ions, adenine nucleobase interaction/coordination-directed biomimetic materials have been fabricated,^[6] and some of them have been consecutively found to exhibit catalytic potential in a number of biomimetic organocatalytic reactions.^[7] However, the application of adenine molecules has never been realized in catalytic reactions for inorganic small molecules.

Recently, we discovered the CO₂ photoactivation potential of adenine nucleobase for the first time^[8] and investigated the reaction mechanism of photocatalytic CO₂-to-HCOOH conversion with the help of metalated adenine-coordinating skeletons originally constructed by Rosi et al.^[6b] On this basis, we unveil the important effect of intermolecular hydrogen-bonding traction of adenine nucleobases on their CO₂ photoreduction activity by establishing a model system containing nearly isomorphous metal-nucleobase frameworks. This biomimetic system involves four metalated adenine-containing architectures, [Co₂(HAD)₂(AD)₂(Aa)₂], (AMOF-1 = bio-MOFs-11; HAD = adenine, Aa = acetic acid), [Co₂(HAD)₂(AD)₂(Pa)₂], (AMOF-2 = bio-MOFs-12; Pa = propionic acid), [Co₂(HAD)₂(AD)₂(Da)₂], (AMOF-3; Da = dimethylacetic acid), and [Co₂(HAD)₂(AD)₂(Ta)₂], (AMOF-4; Ta = trimethylacetic acid), in which adenine molecules as the catalytically active centers possess the same

N. Li, J. He

Department School of Chemical Engineering and Light Industry
Guangdong University of Technology
Guangzhou, Guangdong 510006, China
E-mail: junhe@gdut.edu.cn

S.-J. Yao, Y.-Q. Lan

School of Chemistry
South China Normal University
Guangzhou 510006, P. R. China
E-mail: yqlan@m.scnu.edu.cn

M.-J. Wei

School of Chemistry and Chemical Engineering
Yancheng Institute of Technology
Yancheng, Jiangsu 224051, China

W. Chi

School of Science
Hainan university
No. 58 Renmin Avenue, Meilan District, Haikou 570228, China
E-mail: weijie_chi@hainanu.edu.cn

 The ORCID identification number(s) for the author(s) of this article can be found under <https://doi.org/10.1002/smll.202206724>.

DOI: 10.1002/smll.202206724

coordination environment and spatial arrangement pattern. The main difference between these structures is the coordination of metal ions to aliphatic carboxylic acid ligands with alkyl groups (methyl, ethyl, isopropyl, and *tert*-butyl) of different electron-donating power. Moreover, the coordination of different electron-pushing carboxylic acid ligands leads to a significant change in the strength and environment of hydrogen bonds around adenine nucleobase. In this regard, **AMOF-1–4** can be used as a biomimetic model structural system for systematically studying the effect of hydrogen bond traction on the CO₂ photoreduction activity of adenine. The photocatalytic results show that all AMOFs could achieve highly selective conversion ($\approx 100\%$) of CO₂ to HCOOH, and the yield and activity of the HCOOH product show a nearly steady incremental trend along with increasing electron-pushing abilities of the alkyl groups. Among them, **AMOF-4** coordinated with the most electron-donating trimethylacetic acid has the highest HCOOH production activity with 226.7 $\mu\text{mol g}^{-1} \text{h}^{-1}$. Density functional theory (DFT) calculations demonstrate that the stronger electron-donating ability of the alkyl groups significantly enhances the intermolecular hydrogen bonding traction between carboxyl oxygen and adenine amino group, which leads to stronger adenine-CO₂ interaction energy and then makes the CO₂ activation smoother. This is also the main reason for the improved photocatalytic performance. This work systematically reveals the effect of altered hydrogen bonding environments in the immediate vicinity of adenine nucleobase on its CO₂ photoactivation property and provides additional insights for establishing the corresponding structure–property relationships.

2. Results and Discussion

AMOF-1–4 have very similar parent metalated adenine-containing skeletons, composed of cobalt ions, adenine molecules, and different aliphatic carboxylic acid ligands, and can be synthesized in high yields through similar solvothermal reaction methods. Single crystal X-ray diffraction analysis shows that these metal–nucleobase frameworks crystallize in the same *I*₄/a tetragonal space group (Table S1, Supporting Information). The asymmetric unit contains a crystallographically independent Co^{II} ion, two deprotonated adenine (AD[−]), and aliphatic carboxylic acid (Aa[−]/Pa[−]/Da[−]/Ta[−]) ligands. The same Co1 atoms in different AMOFs exhibit very close tetragonal pyramidal coordination geometries, which are composed of two N atoms (from two AD[−]) and two O atoms (from two carboxylic acid ligands) in the bottom, and one N atom (from another AD[−]) in axial position. Beyond that, the bond lengths and bond angles surrounding the Co1 atoms in these AMOFs also show negligible differences (Tables S2 and S3, Supporting Information). Two adjacent Co1 atoms constitute a paddle-wheel unit (PWU) by sharing four adenine and two carboxylic acid ligands (Figure 1a). Since the PWU makes the coordination environment of the metal ion very saturated and compact, the contact or coordination of any foreign species becomes very difficult. Each adenine molecule is connected to three Co1 atoms of two PWUs by three imino nitrogens, while the remaining naked amino group and neighboring imino nitrogen can form an effective hydrogen bonding network with the nearby aliphatic carboxylic

acid ligand. Based on these structural characteristics, the fact that adenine components (naked amino group and neighboring imino nitrogen), rather than coordination-saturated metal-based PWU unit, can serve as the catalytically active sites to achieve CO₂ photoreduction reaction has been proved in our previous work.^[8] By means of the above-mentioned coordination mode, adjacent PWUs connect with each other by sharing one adenine molecule to form a PWU-based grid along the crystallographic *b*-axis (Figure 1b), and then further expand into a 3D PWU-based framework (Figure 1c). The hydrophobic alkyl moieties of terminal coordinated aliphatic carboxylic acid ligands point into the cavities of these similar AMOFs (Figure 1d–g), for which the main structural difference is that the alkyl groups display reinforced electron-donating effect ($R_4 > R_3 > R_2 > R_1$). As the volume of alkyl groups increases, the aperture sizes of **AMOF-1–4** decrease gradually (Figure 1h–k) and then can hamper the effective adsorption of specific substrate molecules. Moreover, the electron-pushing ability of the alkyl group can significantly affect the charge distribution of the corresponding carboxyl oxygen atom, making it more negatively charged. Notably, the hydrogen bonding network around the adenine molecule is gradually regulated with the increase of alkyl size and negative charge of carboxyl oxygen in the PWU motif. This fact can also be clearly seen from the 3D molecular d_{norm} Hirshfeld surfaces of these AMOFs. As shown in Figure 2a–d, the change in alkyl group volume breeds more intermolecular interactions such as hydrogen bonds and van der Waals forces. Moreover, 2D fingerprint plots display that changes in the alkyl group do modulate the occupancy proportion and strength of the different intermolecular forces as well (Figure 2e–h). In particular, the continuous enhancement of the electron-donating ability of alkyl groups leads to the fact that the hydrogen bonds between carboxyl oxygens and adenine amino groups dominate all intermolecular contacts (Figure 2i–l). Therefore, **AMOF-1–4** can be used as a model system to study how altering the hydrogen bonding microenvironment affects the CO₂ photoactivation performance of the adenine molecule.

Before the CO₂ photoactivation study of adenine nucleobase, the high crystallinity and purity of as-synthesized **AMOF-1–4** crystals were first confirmed by their identical experimental and simulated powder X-ray diffraction (PXRD) patterns (Figure S1, Supporting Information). Thermogravimetric analysis curves showed that these metal–nucleobase matrices can maintain good structural stability before 300 °C (Figure S2, Supporting Information). Moreover, based on a large number of Lewis base sites (naked amino groups and imino nitrogens) present in the microporous structures of **AMOF-1–4**, the CO₂ adsorption isotherms were measured at 298 K and under 1 atm by using activated samples to evaluate their CO₂ adsorption capacity (Figure S3, Supporting Information). Due to the differences in pore size, the CO₂ uptakes of these biomimetic frameworks were found to be 180.34 (**AMOF-1**), 172.67 (**AMOF-2**), 125.46 (**AMOF-3**) and 73.93 cm³ g^{−1} (**AMOF-4**). It is worth noting that, compared with the colorless organic ligands, **AMOF-1–4** crystals all appear black (Figure S4, Supporting Information), suggesting that the strong ligand-to-metal charge transfer endows them with superior light-harvesting ability. Moreover, the UV–vis light absorption spectra also proved that these biomimetic adenine-containing architectures all exhibited a similar wide

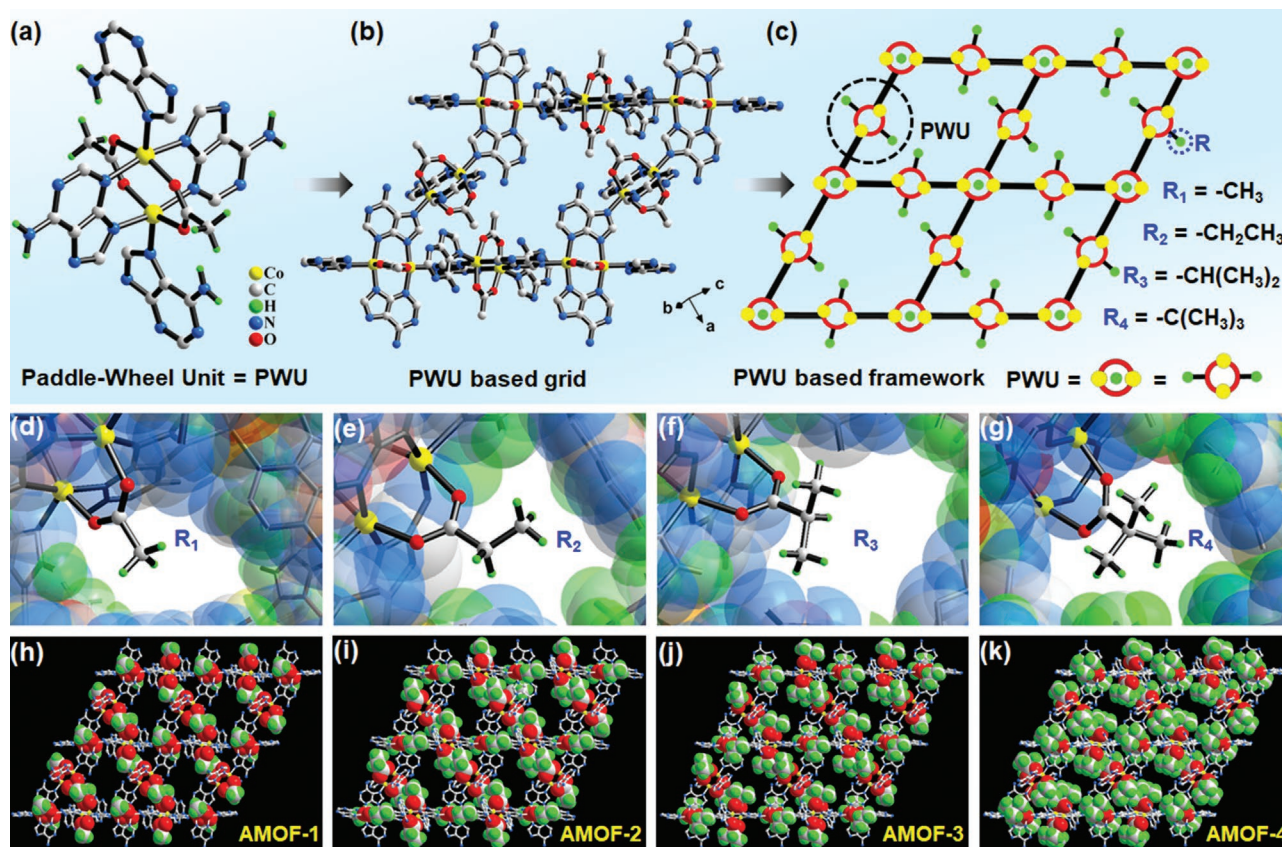


Figure 1. Crystal structures of AMOFs. a) The composition of PWU in **AMOF-1**, which also exists in **AMOF-2-4** but has different aliphatic carboxylic acid ligands. b) The PWU-based grid of AMOFs (e.g., **AMOF-1**). c) The schematic PWU-based framework of AMOFs. d–g) The hydrophobic alkyl moieties of terminal coordinated carboxylic acid ligands in PWU of AMOFs. h–k) The 3D networks of **AMOF-1-4** where carboxylic acid ligands with different terminal electron-donating alkyl groups are presented in space-filling.

light absorption range with distinct light absorption peaks at ≈ 440 and 570 nm (Figure 3a). Using **AMOF-4** as a representative catalyst, the calculations demonstrated that the high energy absorption peak (≈ 440 nm) of **AMOF-4** mainly originates from the n electron in adenine to σ^* in the metal center, and the transition of π electron in adenine to σ^* in the metal center leads to the low energy absorption peak (≈ 570 nm) (Figure S5, Supporting Information). According to their Tauc plots, the band gaps (E_g) were calculated to be 1.62 (**AMOF-1**), 1.68 (**AMOF-2**), 1.52 (**AMOF-3**), and 1.79 eV (**AMOF-4**) (Figure 3b), indicating that **AMOF-1-4** have the characteristics of the semiconductor. To determine the energy band distribution of these semiconductor-like compounds, Mott–Schottky electrochemical measurements were performed at frequencies of 500, 1000, and 1500 Hz.^[9] As shown in Figure 3c and Figures S6–S8, Supporting Information, the high-lying lowest unoccupied molecular orbital (LUMO) positions of **AMOF-1-4** were evaluated to be -0.75 , -0.83 , -0.66 , and -0.93 V (vs NHE, pH = 7), respectively, while their corresponding highest occupied molecular orbital (HOMO) positions were deduced to be 0.87, 0.85, 0.86, and 0.86 V (vs NHE, pH = 7) (Figure 3c). Considering the deep LUMO levels of these metalated adenine-containing skeletons, they are thermodynamically active for CO₂ reduction reactions (CO₂RR) such as the production of possible product HCOOH (-0.58 V vs NHE) (Figure 3d).^[10]

Given the characteristics of superior light-harvesting ability and suitable energy level structure distribution, these biomimetic metal–nucleobase frameworks were used as photocatalysts to carry out CO₂RR. The visible-light-driven photocatalytic reaction system with the activated **AMOF-1-4** was conducted in wet acetonitrile with triethylamine (TEA) as an electron donor under a pure CO₂ atmosphere (1 atm, 293 K), in the absence of any photosensitizer and noble-metal cocatalysts (experimental details are described in Supporting Information).^[11] As shown in Figure 4a, all these biomimetic adenine-containing architectures during the reaction process showed high photocatalytic selectivity (close to 100%) for CO₂-to-HCOOH conversion, while only the trace amount of competitive gaseous reduction product (CO) was observed by gas chromatography (GC). With the prolonged irradiation time, the output (the average of parallel experiments) of the main reduction product (HCOOH) of **AMOF-1-4** detected by ion chromatography showed an almost linear growth trend, and the average product yields corresponding to the catalysts followed the order of **AMOF-4** > **AMOF-3** > **AMOF-2** > **AMOF-1**. After 6 h of photocatalytic reaction, the total HCOOH production of **AMOF-4** reached ≈ 6.8 μmol (226.7 $\mu\text{mol g}^{-1} \text{h}^{-1}$), which was almost 1.7 times that of **AMOF-3** (4.1 μmol , 136.7 $\mu\text{mol g}^{-1} \text{h}^{-1}$), 3.1 times that of **AMOF-2** (2.2 μmol , 73.3 $\mu\text{mol g}^{-1} \text{h}^{-1}$), and 13.6 times that of **AMOF-1**

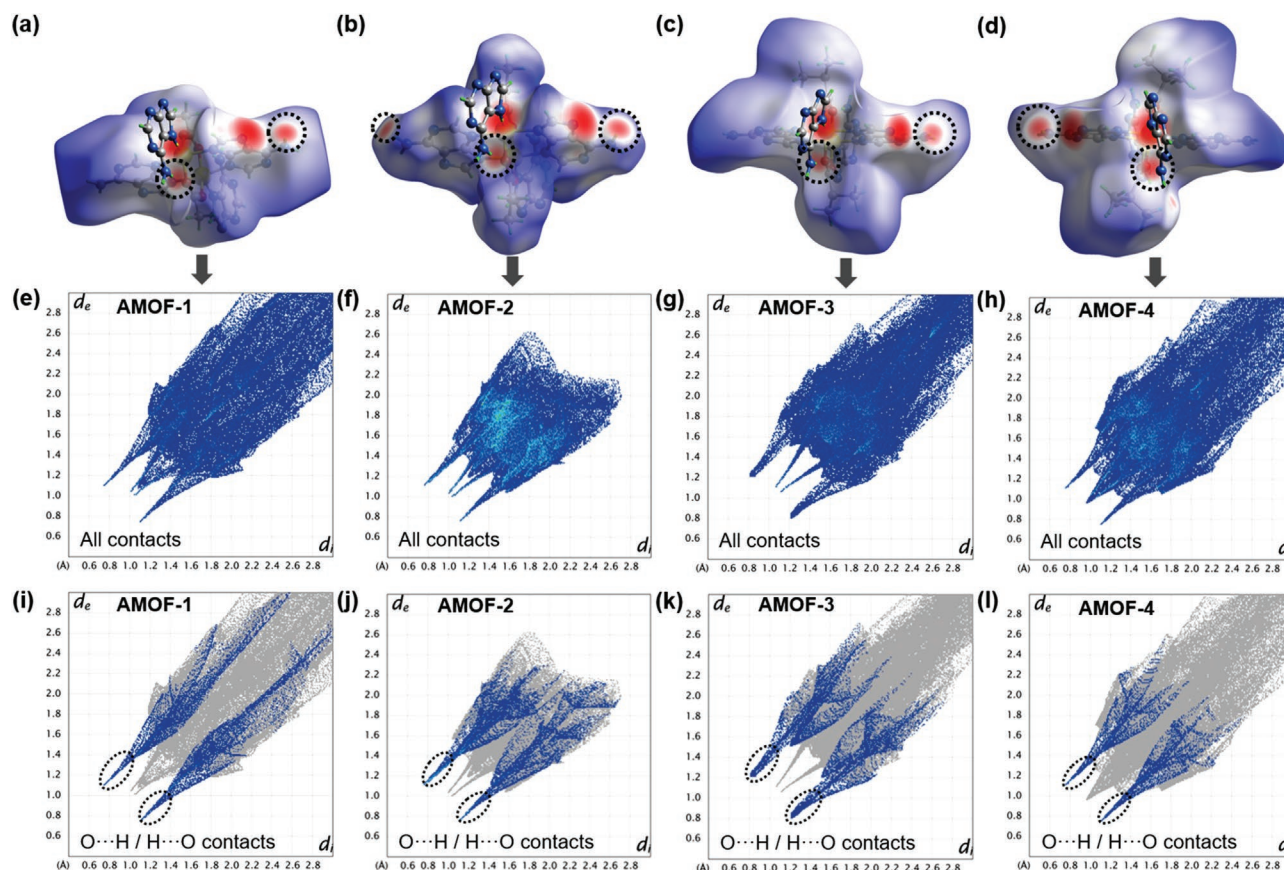


Figure 2. a–d) View of the 3D molecular d_{norm} Hirshfeld surface for PWU in AMOFs. The dashed circles mainly display the contributions of the intermolecular hydrogen bonds between the amino group on adenine and the oxygen atom on carboxylic acid. e–h) 2D fingerprint plots of all contacts for PWU in AMOFs. i–l) 2D fingerprint plots of intermolecular O–H / H–O contacts in AMOFs.

(0.5 μmol , 16.7 $\mu\text{mol g}^{-1} \text{h}^{-1}$), respectively (Figure 4a). In these biomimetic adenine-based frameworks, the photocatalytic performance was gradually improved along with the enhancing electron-donating powers of the alkyl groups (methyl, ethyl, isopropyl, and *tert*-butyl) of the coordinated aliphatic carboxylic acid ligands. Of note, the catalytic activities of AMOF-1–4 could be further enhanced when the photosensitizer (e.g., $[\text{Ru}(\text{bpy})_3] \text{Cl}_2 \cdot 6\text{H}_2\text{O}$) is involved in the catalytic reaction, resulting in an obvious increase in the final HCOOH yield. This phenomenon is mainly attributed to the better contact and more efficient photoinduced charge transfer between homogeneous photosensitizer molecules and adenines in AMOFs.

Photoluminescence (PL) and time-resolved fluorescence decay techniques, transient photocurrent measurements, and electrochemical impedance spectroscopy (EIS) were conducted to investigate the roles of efficient photoexcitation, charge separation, and migration behaviors in the enhancement of photocatalytic performance of AMOFs. However, we did not detect any significant fluorescence/phosphorescence emission and lifetime decay signals for these metal-adenine architectures when excited with different wavelengths (in the range of 250–480 nm) of light, which may result from the low radiation rate and high non-radiation rate (Figure S9, Supporting Information). Therefore, transient photocurrent measurement was further performed to examine the photoinduced electron transfer

efficiency (Figure 4b).^[12] Under periodic light irradiation and shutdown, AMOF-1–4 presented sharp current responses as shown in Figure 4b. After switching multiple rounds, the photocurrent intensities of AMOF-1–2 are close, while the photocurrent intensities of AMOF-3–4 are similar. Thus, it is evident that AMOF-3–4 has a slightly higher photocurrent intensity compared to AMOF-1–2, implying that AMOF-3–4 indeed has a better-photogenerated charge separation capability than AMOF-1–2. Moreover, EIS spectra of these biomimetic catalysts also exhibit gradually decreasing semicircle radius in Nyquist plots (AMOF-1 > AMOF-2 > AMOF-3 > AMOF-4), suggesting that the interfacial charge transfer process of AMOF becomes more and more faster (AMOF-1 < AMOF-2 < AMOF-3 < AMOF-4) (Figure S10, Supporting Information). Combining the above photoelectrochemical characterizations, it can be inferred that these catalysts basically exhibit a trend of AMOF-4 > AMOF-3 > AMOF-2 > AMOF-1 in terms of photogenerated charge separation and transfer ability. To further validate the exciton separation (or charge separation) efficiency of AMOFs, time-dependent DFT (TD-DFT) was also employed to calculate the exciton binding energies (E_b) in the excited state. In general, a small E_b results in high exciton separation efficiency. The corresponding E_b values were determined to be 2.828 (AMOF-1), 2.495 (AMOF-2), 2.404 (AMOF-3), and 1.646 eV (AMOF-4), respectively (Figure S11, Supporting Information). This result

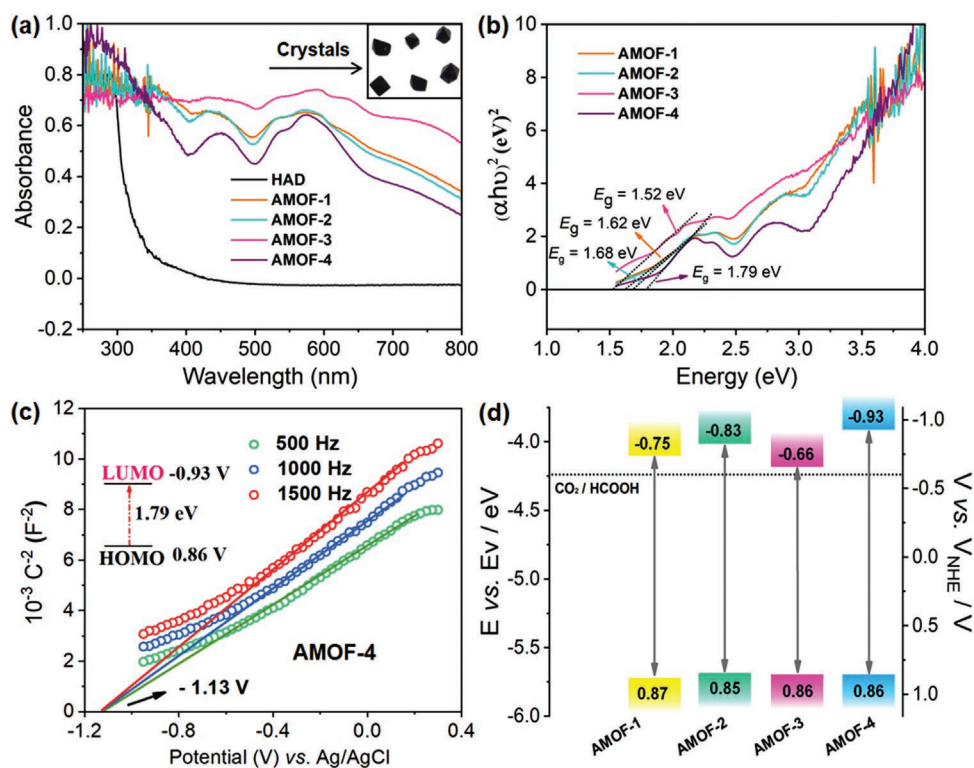


Figure 3. Optical characterization and energy levels distribution of AMOFs. a) UV-vis absorption spectra of AMOFs and adenine ligand. b) Band gap energy (E_g) analysis of AMOFs. The intersection of the baseline and the slant dashed line equals the band gap. c) Mott-Schottky plot for **AMOF-4** in 0.2 M Na_2SO_4 aqueous solution. Inset is the energy diagram of the HOMO and LUMO levels of **AMOF-4**. d) Energy bandgap diagrams of AMOFs with respect to the CO_2 -to- HCOOH conversion. The electron volts (eV, left y-axis) are converted to electrochemical energy potentials in volts (V, right y-axis) according to which 0 V versus reversible hydrogen electrode (RHE) equals -4.44 eV versus vac (vacuum level). Then, the RHE potentials are further converted to NHE (pH = 7) according to E (vs NHE, pH = 7) = E (vs RHE) $- 0.0591 \times 7$.

also suggested that these biomimetic catalysts displayed a steadily improved exciton separation efficiency (**AMOF-1** < **AMOF-2** < **AMOF-3** < **AMOF-4**), which is consistent with our experimental data.

In addition, we executed photocatalytic reactions with different monochromatic light (380, 420, 520, and 600 nm) wavelength excitations. After the reactions, the wavelength-dependent quantum efficiencies (QE) corresponding to the different catalysts were calculated (please see the QE measurement in Supporting Information). Since these adenine-containing biomimetic catalysts have significantly different light absorption intensities in the UV-vis region, their quantum efficiencies corresponding to different wavelengths are also different. It is obvious that these wavelength-dependent quantum efficiencies do not well match completely the optical absorption spectra of the catalysts. However, it is well known that the final photocatalytic performance is often determined by a comprehensive result of a variety of influence factors such as catalyst- CO_2 interaction (the first step for CO_2 RR), light-harvesting, the ability of photoinduced charge separation and transfer. Therefore, we think these results are relatively reasonable. From the simple summation of quantum efficiencies, the corresponding total yields of HCOOH also follow the trend of **AMOF-4** > **AMOF-3** > **AMOF-2** > **AMOF-1**.

To confirm that these biomimetic MOFs are indeed active for photocatalytic CO_2 RR, a series of control experiments were

conducted in the absence of adenine-based photocatalysts, light illumination, or CO_2 atmosphere. It was found that no reduction products could be detected by IC and GC in these control experiments (Tables S4 and S5, Supporting Information). These results clearly proved the photocatalytic activity of **AMOF-1-4** for CO_2 -to- HCOOH conversion. In addition, the effect of mass variation (2, 5, 10, 20, and 30 mg) on the photocatalytic performance was further investigated under the same reaction conditions with **AMOF-4** as a representative catalyst.^[13] As shown in Figure 4c, the total yield of HCOOH after 6-h illumination continued to increase with the amount of catalyst input, but the photocatalytic activity increased initially and dropped when the amount of catalyst input is larger than 5 mg. In the present photocatalytic reaction system, 5 mg represents the optimal amount of catalyst to give the best reduction product yield and photocatalytic reaction activity. Subsequently, we used the optimized catalyst amount (5 mg) to evaluate the photocatalytic stability of these adenine-based biomimetic frameworks. After undergoing at least four rounds of recycling experiments, **AMOF-1-4** nearly maintained their initial photocatalytic activities (Figure 4d). The observable slight decay to the HCOOH yield is mainly attributed to the mass loss of photocatalysts during recovery. The resultant reaction filtrates without photocatalyst solids did not show any obvious UV-vis absorption signal (Figure S12, Supporting Information), which excluded that the photocatalytic activity stems from the decomposed

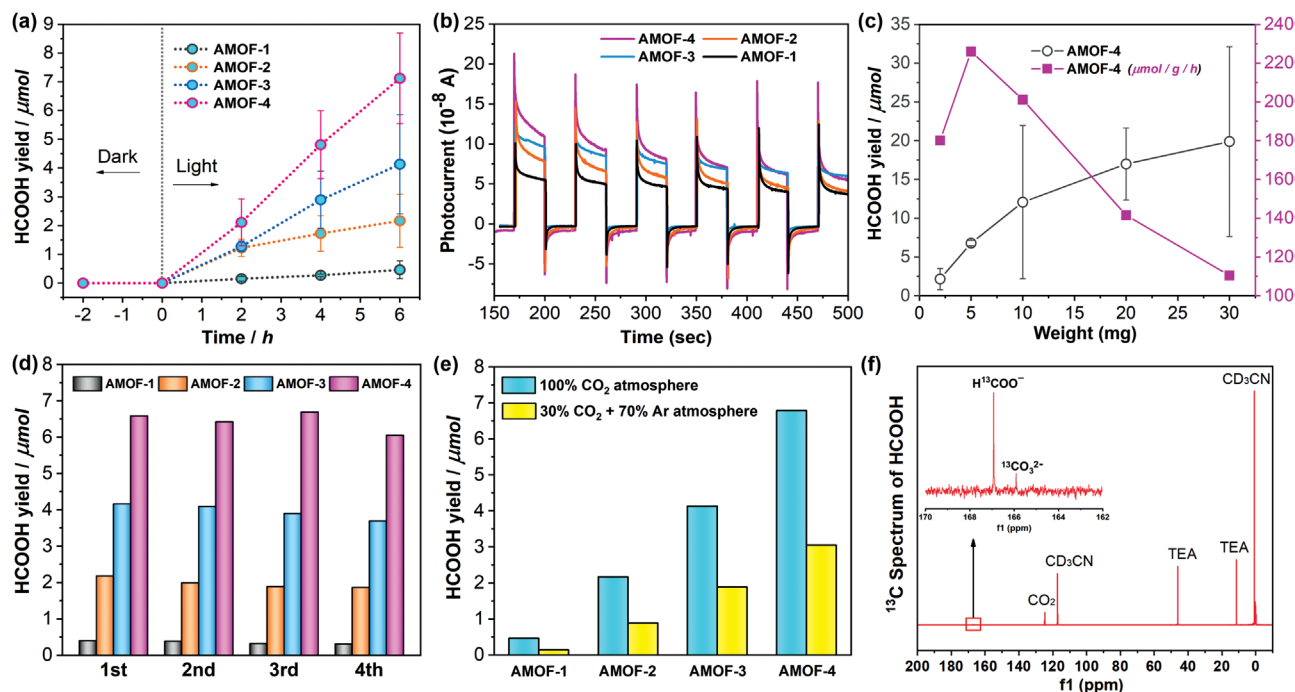


Figure 4. Photochemical characterizations and isotopic experiment for CO₂RR. a) Time-dependent HCOOH yield of AMOFs. b) Transient photocurrent response of AMOFs. A Xenon light (300–1100 nm) as the light source was applied for photocurrent measurement, and 0.5 M Na₂SO₄ aqueous solution was used as the electrolyte. c) Relationship between yield and rate of HCOOH production in different quality of AMOF-4. d) Yields of HCOOH for AMOF photocatalysts in four continuous runs. e) Comparison of the HCOOH generation of AMOFs under different reaction atmospheres, with 100% CO₂ and 30% CO₂ (+ 70% Ar). f) ¹³C NMR spectrum of reaction solution catalyzed with AMOF-4 photocatalyst under ¹³CO₂ atmosphere.

active components of catalysts. Moreover, no significant changes occurred on IR spectra and PXRD patterns of AMOF-1–4 performed before and after CO₂RR, confirming the heterogeneous catalytic nature and structural stability of these metal-nucleobase backbones (Figures S13 and S14, Supporting Information). Beyond that, we also performed the identical CO₂RR with AMOF-1–4 photocatalysts under a low-concentration CO₂ (30% CO₂ and 70% Ar) atmosphere to verify their practical application potential (Figure 4e). Obviously, compared with the condition of a pure CO₂ atmosphere, these biomimetic catalysts can still show a certain photocatalytic activity and the same trend in the yield of reduction product (AMOF-4 > AMOF-3 > AMOF-2 > AMOF-1). On this basis, we also carried out the isotopic ¹³CO₂ experiment (¹³CO₂ atmosphere) under identical CO₂RR conditions in the presence of photosensitizer to validate the carbon source origin of the produced HCOO⁻. As shown in Figure 4f, the H¹³COO⁻ product signal at 166.7 ppm was clearly observed from the ¹³C NMR spectrum, which is consistent with the previously reported works.^[14] By contrast, no detectable HCOO⁻ signal could be found on the ¹³C NMR spectrum when the ¹²CO₂ atmosphere was employed in an identical reaction system (Figure S15, Supporting Information). These results unambiguously indicated that biomimetic AMOF-1–4 are indeed active for visible-light-driven CO₂-to-HCOOH conversion. In addition, as with other crystalline catalysts,^[15] the well-defined crystal structure information of AMOF-1–4 can provide an important foundation for studying the mechanism of CO₂ photoactivation and establishing the corresponding structure–property relationships.

We have previously demonstrated that adenine nucleobase can complete the photocatalytic conversion of CO₂ molecules through the synergy of the amino group and neighboring imino nitrogen. CO₂ molecule first interacts strongly with the amino group (Lewis-basic site) of adenine through hydrogen bonding interaction and then accepts the proton-coupled electrons transferred from the neighboring imino nitrogen for subsequent activation process and reduction reaction (Figure 5).^[8] To investigate the CO₂ photoactivation performance of adenine biomolecule in depth, in this work, we establish an adenine-containing biomimetic model system, in which the adenine molecules share the same coordination pattern and spatial arrangement, except that the metal ions are coordinated with different terminal aliphatic carboxylic acid ligands. Because of the increased size and enhanced electron-donating capacity of the alkyl groups (methyl, ethyl, isopropyl, and *tert*-butyl) of these carboxylic acid ligands, the hydrogen bonding microenvironment around the catalytically active adenine molecule is significantly and sequentially altered. Moreover, the relevant conclusion drawn from the experimental results seems to be that the stronger the electron-donating ability of the aliphatic carboxylic acid ligand, the better the photocatalytic performance of AMOF exhibits. Consequently, it is essential to explore the origin of the improved CO₂ photoactivation performance of adenine for its subsequent artificial catalytic applications.

The DFT calculations were employed to understand the differences in the photocatalytic performance of AMOF-1–4. The geometries of AMOF-1–4 were optimized at PBE/Def2SVP level using Gaussian 16 code. The initial configurations were from

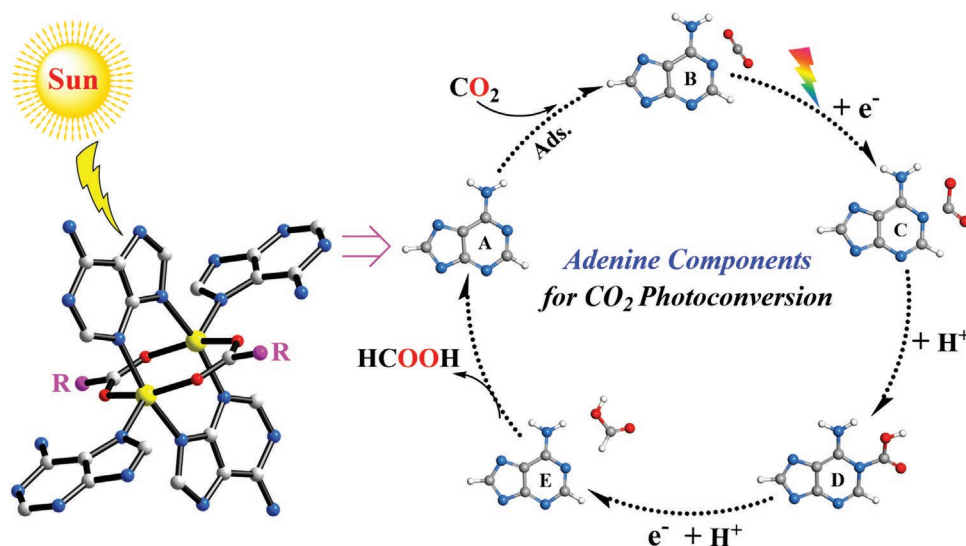


Figure 5. Photocatalytic CO₂-to-HCOOH reduction mechanism of adenine molecules in AMOF-1-4.

their crystal structures. Frequency analysis was performed to confirm that we obtained molecular structures located at the local minima on the potential energy surfaces. The van der Waals correction (D3) was included in all calculations. Calculated results showed that the terminal alkyl groups had almost no effect on the electronic properties of AMOF-1-4. In this regard, they had similar distributions of frontier molecular orbitals (FMO), the HOMOs were located on the two contrary adenines, and the LUMOs were distributed on the two contrary adenines and central metal units (Figure 6a). In addition, AMOF-1-4 also displayed similar molecular electrostatic potential surfaces (EPS). Specifically, the hydrogen atoms led to the positive EPS, and the nitrogen atoms resulted in the negative EPS. Interestingly, we showed that the maximum EPS values increased slightly with the size of terminal alkyl groups (Figure 6b). The difference in EPS may be derived from the electron-donating ability of terminal alkyl groups. For example, compared with the methyl group in AMOF-1, the *tert*-butyl group in AMOF-4 with a stronger electron-donating ability caused the oxygen atom on the carboxyl group to possess more negative charge, which induced a more positive electrostatic potential around the amino group (Figure 7).

The previous report has affirmed that CO₂ adsorbed onto the adenine-based systems through the interaction of intermolecular hydrogen bonds. Hence, we speculated that the hydrogen bond interaction gradually strengthened from AMOF-1 to AMOF-4. To verify the speculation, we optimized the geometries of the CO₂ and AMOF-1-4 complexes (AMOF-1-CO₂ – AMOF-4-CO₂). Indeed, the hydrogen bond lengths shortened in sequence from AMOF-1-CO₂ to AMOF-4-CO₂, indicative of the enhanced interaction of intermolecular hydrogen bonds (Figure 6c). Besides, we also showed the weak van der Waals interactions of carbon atoms in CO₂ and the nitrogen atoms in adenines due to the short non-covalent bond distances (≈ 2.710 Å). To further verify these hydrogen bonds and van der Waals interaction, we employed the interaction region indicator (IRI) real space function to investigate these interactions in AMOF-1-CO₂ – AMOF-4-CO₂. The IRI can display the strong

chemical bonds and weak interaction regions equally well. The noteworthy van der Waals (green regions) and hydrogen bond interactions (blue regions) were found in AMOF-1-CO₂ – AMOF-4-CO₂. Besides, the calculated interaction energies (ΔE) of CO₂ and AMOF-1-4 were 34.1, 34.3, 34.3, and 35 kJ mol⁻¹, respectively (Figure 6c). Compared with the van der Waals interactions, the hydrogen bond interactions played a more critical role in increasing the intermolecular interactions due to short O–H distances. According to these calculated results and experimental data, we demonstrated that the large size of terminal alkyl groups caused the strong intermolecular interactions, especially hydrogen bonding interactions, of CO₂ and AMOF-1-4, which was the molecular origin that AMOF-4 has the best photocatalytic performance in AMOF-1-4.

In addition, to further demonstrate the importance of intermolecular hydrogen bonding traction, DFT calculations are also employed to evaluate the interaction energies between adenine and other inorganic small molecules. Using AMOF-1 and AMOF-4 as representative catalysts, we calculate the interaction energies between adenine and different types of small molecules, such as CO (linear polar molecule) and SO₂ (nonlinear polar molecule), which have different molecular configurations or/and polarities compared with CO₂ (linear nonpolar molecule). The calculations show that the CO molecule is hard to be adsorbed on adenine and even escape, despite the presence of amino traction. As shown in Figure 8a,b, long interaction distances (with $\Delta E \approx 0$ KJ mol⁻¹) mean that these adenine-containing biomimetic catalysts do not have sufficient capacity to capture CO, which may originate from the tiny positive charge of C atom in CO as compared with CO₂. By contrast, the SO₂ molecule can be adsorbed easily on the adenine, and the interaction energy (ΔE) of AMOF-4-SO₂ is larger than that of AMOF-1-SO₂ (Figure 8c,d). Moreover, the ΔE between AMOF-1/AMOF-4 and SO₂ is also much higher than that of AMOF-1/AMOF-4 and CO₂, which is attributed to the higher positive S atom in SO₂. Given that the environmental issues originated from CO₂ (greenhouse gas) and SO₂ (atmospheric pollutants), we believe that the conclusions demonstrated in this work can

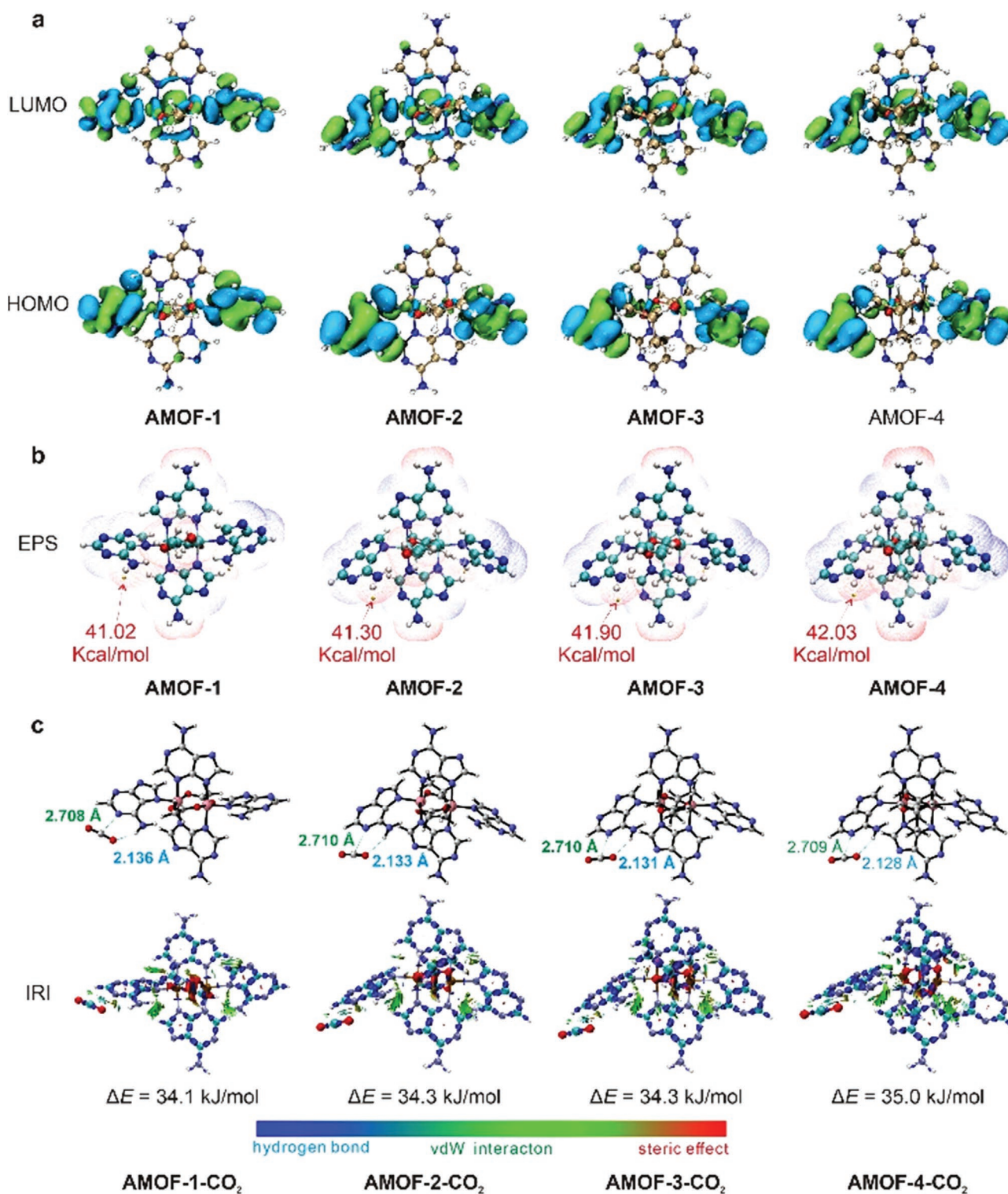


Figure 6. a) The distributions of HOMOs and LUMOs in AMOF-1–4, b) the molecular electrostatic potential surfaces (electron density isosurfaces of 0.001 au) and the maximum EPS values, c) the molecular structures and key bond distances of AMOF-1-CO₂–AMOF-4-CO₂, and the isosurface maps of IRI and intermolecular interaction energies (ΔE) for AMOF-1-CO₂–AMOF-4-CO₂. All calculations were carried out at PBE/Def2SVP level.

provide new inspiration and important insights for the future application of adenine nucleobase to other possible chemical/physical reactions involving these small molecules.

In our previous work, we discovered for the first time that adenine biomolecules rather than conventional metal centers can serve as catalytic sites for CO₂ photoreduction reactions

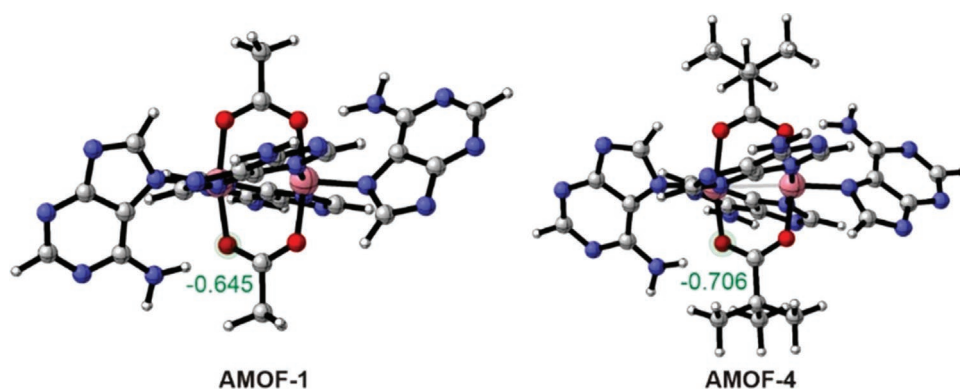


Figure 7. The calculated modified Mulliken atom charge at PBE/Def2SVP level.

through two biomimetic metal–nucleobase framework catalysts. Moreover, the catalytic conversion of the CO_2 molecule was shown to be accomplished by the synergistic interaction of the amino group and the neighboring imino nitrogen of the adenine molecule, which means a new catalytic strategy for efficient CO_2 photoconversion. In view of the new potential application of the adenine molecule discovered in the previous work, we hope that the next step will be to clearly identify the underlying structure–property relationships affecting its

photocatalytic activity, which can further advance its application to other types of catalytic reactions. However, due to the very different structures and photocatalytic reaction conditions of the catalysts constructed in the previous work, we were unable to investigate the main structural inducements influencing the CO_2 photoreduction activity of adenine molecules systematically and clearly. This fact severely limits the subsequent design, synthesis, and application of more effective adenine-based photocatalysts, as well as the improvement of photocatalytic

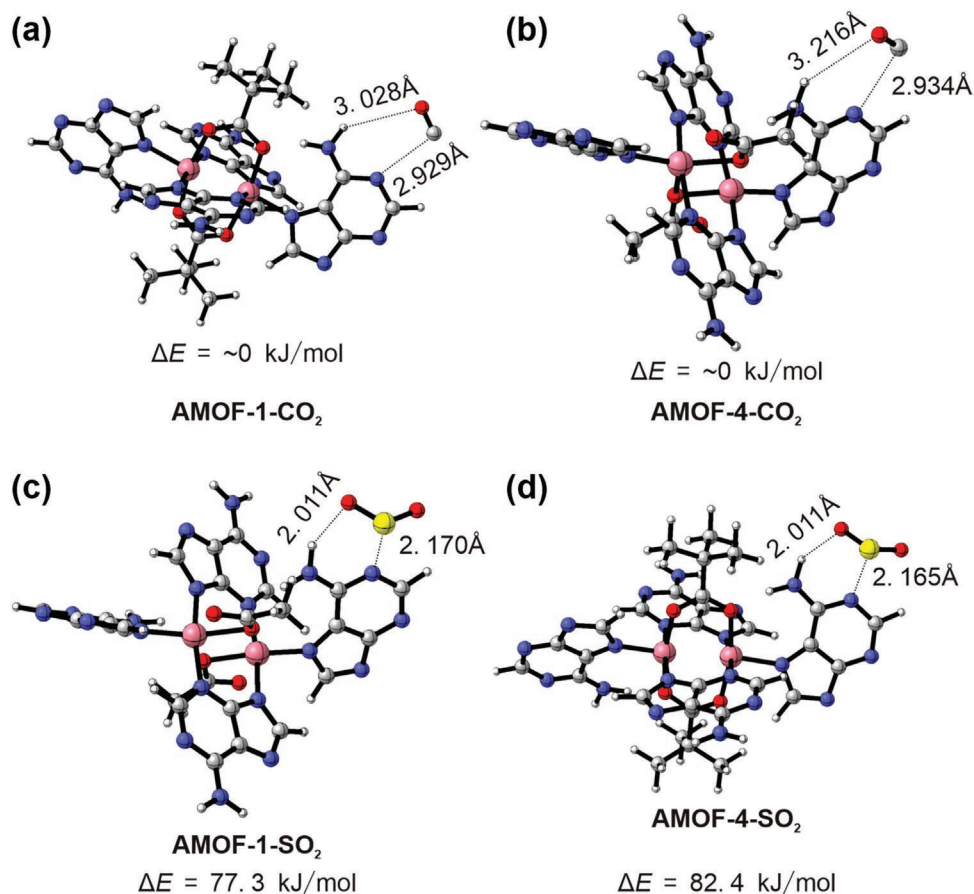


Figure 8. a–d) The molecular structures and key bond distances of AMOF-1- CO/SO_2 and AMOF-4- CO/SO_2 , and the isosurface maps of IRI and intermolecular interaction energies (ΔE) for AMOF-1- SO_2 and AMOF-4- SO_2 .

performance. To effectively address these issues, we elaborately establish an adenine-containing model catalyst system in this work. It allows us to explore the precise effects on photocatalytic performance as the structural microenvironment in which the active adenine molecule is located changes regularly. Through this work, we find that the stronger electron-donating ability of the alkyl groups significantly enhances the intermolecular hydrogen bonding traction between carboxyl oxygen and adenine amino group, which leads to stronger adenine-CO₂ interaction energy and then makes the CO₂ activation smoother. This is also the main reason and first step (CO₂ adsorption) for improved photocatalytic performance. In this way, the structural features of the model catalysts, experimental characterizations, and theoretical calculations were effectively combined to clearly confirm that the main factor affecting the CO₂ photoreduction activity of adenine molecules is the intermolecular hydrogen bonding traction. Moreover, this conclusion is in fact consistent with the catalytic role that adenine molecules usually play in the living environment, that is, using the surrounding hydrogen-bonding microenvironment to modulate biocatalytic processes and properties. This work systematically reveals the effect of altered hydrogen bonding environments surrounding adenine nucleobase on artificially manipulated CO₂ photoactivation properties and provides important insights for establishing the corresponding structure–property relationships.

Since adenine nucleobase is an organic molecule, we also consider that this model system may have the following advantages as compared to inorganic photocatalysis in terms of CO₂ photoactivity: i) the clear crystal structure information of these metal–nucleobase frameworks are very helpful to accurately identify the catalytic active sites and establish the structure–performance relationships, which are essential for the modulation and enhancement of photocatalytic performance; ii) this model system has low-toxic biomolecules as the main photocatalytic active centers, which allows the catalytic reaction to proceed in a relatively green manner; iii) this model system can serve as a good platform to investigate the effect of changes in intermolecular hydrogen-bonding traction around the catalytic active site on the photoactivation of CO₂; iv) this model system could provide insights for the development of more active biomolecule-based biomimetic catalysts for CO₂ photoactivation.

3. Conclusion

In summary, we have developed a model metal-adenine architectures system (AMOF-1–4) in which the adenine molecules exhibit the same coordination pattern and spatial arrangement except that the metal ions are coordinated to different aliphatic carboxylic acid ligands. As the terminal alkyl groups (methyl, ethyl, isopropyl, and *tert*-butyl) of the carboxylic acid ligands increase in electron-donating capacity, the hydrogen bonding environment around the active adenine molecules (especially the intermolecular hydrogen bonding interactions between the carboxyl oxygen and amino group) is altered stepwise and leads to an ordered enhancement of CO₂-to-HCOOH photoreduction performance. In this regard, we use this model system to reveal for the first time the important influence of

intermolecular hydrogen bonding traction on the CO₂ photoactivation potential of adenine nucleobase. The photocatalytic results combined with DFT theoretical calculations show that the enhanced electron-donating ability of the terminal alkyl group of the aliphatic carboxylic acid ligand can improve the electrostatic potential between carboxyl oxygen and amino group, which leads to an increase in the adenine-CO₂ interaction energy and contributes to a more rapid CO₂ activation process. Importantly, the effect of hydrogen bonding traction on CO₂ photoactivation of adenine biomolecule revealed by this work can be further applied to more small molecule catalytic reactions.

Supporting Information

Supporting Information is available from the Wiley Online Library or from the author.

Acknowledgements

N.L., S.-J.Y., and M.-J.W. contributed equally to this work. This work was financially supported by the China Postdoctoral Science Foundation (2021M700877 and No. 15 Special Fund (In-Station), 2022T150143), the National Natural Science Foundation of China (No. 22201046, 21871061, and 21871141), the Local Innovative and Research Teams Project of Guangdong Pearl River Talents Program (2017BT01Z032), the Research Start-up Fund Project of Hainan University (Nos. RZ2200001217 and RZ2200001216), and Tianjin University-Hainan University Independent Innovation Fund (RZ2200003795).

Conflict of Interest

The authors declare no conflict of interest.

Data Availability Statement

The data that support the findings of this study are available from the corresponding author upon reasonable request.

Keywords

adenine nucleobase, CO₂ photoactivation, hydrogen bonding, metal–organic frameworks

Received: November 2, 2022

Revised: November 12, 2022

Published online:

- [1] a) J. Shi, Y. Wu, S. Zhang, Y. Tian, D. Yang, Z. Jiang, *Chem. Soc. Rev.* **2018**, *47*, 4295; b) L. Que, W. B. Tolman, *Nature* **2008**, *455*, 333; c) T. R. Cech, B. L. Bass, *Annu. Rev. Biochem.* **1986**, *55*, 599.
- [2] a) R. A. Sheldon, D. Brady, M. L. Bode, *Chem. Sci.* **2020**, *11*, 2587; b) R. A. Sheldon, J. M. Woodley, *Chem. Rev.* **2018**, *118*, 801.
- [3] A. Das, C. Hessin, Y. Ren, M. Desage-El Murr, *Chem. Soc. Rev.* **2020**, *49*, 8840.
- [4] S. Sivakova, S. J. Rowan, *Chem. Soc. Rev.* **2005**, *34*, 9.

- [5] a) S. Verma, A. K. Mishra, J. Kumar, *Acc. Chem. Res.* **2010**, *43*, 79; b) Y. I. Kuzmin, C. P. Da Costa, J. W. Cottrell, M. J. Fedor, *J. Mol. Biol.* **2005**, *349*, 989.
- [6] a) A. Sikder, C. Esen, R. K. O'Reilly, *Acc. Chem. Res.* **2022**, *55*, 1609; b) T. Li, D.-L. Chen, J. E. Sullivan, M. T. Kozlowski, J. K. Johnson, N. L. Rosi, *Chem. Sci.* **2013**, *4*, 1746; c) R. K. Gupta, M. Riaz, M. Ashafaq, Z.-Y. Gao, R. S. Varma, D.-C. Li, P. Cui, C.-H. Tung, D. Sun, *Coord. Chem. Rev.* **2022**, *464*, 214558; d) L.-L. Xu, H.-F. Zhang, M. Li, S. W. Ng, J.-H. Feng, J.-G. Mao, D. Li, *J. Am. Chem. Soc.* **2018**, *140*, 11569.
- [7] a) C. E. Paul, I. W. C. E. Arends, F. Hollmann, *ACS Catal.* **2014**, *4*, 788; b) Y. Rachuri, J. F. Kurisingal, R. K. Chitumalla, S. Vuppala, Y. Gu, J. Jang, Y. Choe, E. Suresh, D.-W. Park, *Inorg. Chem.* **2019**, *58*, 11389; c) Y. Lyu, J. Tian, J. Li, P. Chen, K. Pu, *Angew. Chem., Int. Ed.* **2018**, *57*, 13484.
- [8] N. Li, J. Liu, J. J. Liu, L. Z. Dong, Z. F. Xin, Y. L. Teng, Y. Q. Lan, *Angew. Chem., Int. Ed.* **2019**, *58*, 5226.
- [9] a) H.-Q. Xu, J. Hu, D. Wang, Z. Li, Q. Zhang, Y. Luo, S.-H. Yu, H.-L. Jiang, *J. Am. Chem. Soc.* **2015**, *137*, 13440; b) H. X. Zhang, Q. L. Hong, J. Li, F. Wang, X. Huang, S. Chen, W. Tu, D. Yu, R. Xu, T. Zhou, J. Zhang, *Angew. Chem., Int. Ed.* **2019**, *58*, 11752; c) K. Maeda, K. Sekizawa, O. Ishitani, *Chem. Commun.* **2013**, *49*, 10127.
- [10] a) Y. Tamaki, T. Morimoto, K. Koike, O. Ishitani, *Proc. Natl. Acad. Sci. U. S. A.* **2012**, *109*, 15673; b) T.-C. Zhuo, Y. Song, G.-L. Zhuang, L.-P. Chang, S. Yao, W. Zhang, Y. Wang, P. Wang, W. Lin, T.-B. Lu, Z.-M. Zhang, *J. Am. Chem. Soc.* **2021**, *143*, 6114.
- [11] a) H. Zhang, J. Wei, J. Dong, G. Liu, L. Shi, P. An, G. Zhao, J. Kong, X. Wang, X. Meng, J. Zhang, J. Ye, *Angew. Chem., Int. Ed.* **2016**, *55*, 14310; b) H. Takeda, K. Ohashi, A. Sekine, O. Ishitani, *J. Am. Chem. Soc.* **2016**, *138*, 4354.
- [12] a) R. Long, Y. Li, Y. Liu, S. Chen, X. Zheng, C. Gao, C. He, N. Chen, Z. Qi, L. Song, J. Jiang, J. Zhu, Y. Xiong, *J. Am. Chem. Soc.* **2017**, *139*, 4486; b) L. Wang, J. Wan, Y. Zhao, N. Yang, D. Wang, *J. Am. Chem. Soc.* **2019**, *141*, 2238; c) X. Yu, Z. Yang, B. Qiu, S. Guo, P. Yang, B. Yu, H. Zhang, Y. Zhao, X. Yang, B. Han, Z. Liu, *Angew. Chem., Int. Ed.* **2019**, *58*, 632; d) Y. Wang, Z. Zhang, L. Zhang, Z. Luo, J. Shen, H. Lin, J. Long, J. C. S. Wu, X. Fu, X. Wang, C. Li, *J. Am. Chem. Soc.* **2018**, *140*, 14595; e) C. Bie, B. Zhu, F. Xu, L. Zhang, J. Yu, *Adv. Mater.* **2019**, *31*, 1902868.
- [13] a) S. Wang, W. Yao, J. Lin, Z. Ding, X. Wang, *Angew. Chem., Int. Ed.* **2014**, *53*, 1034; b) L. Z. Dong, L. Zhang, J. Liu, Q. Huang, M. Lu, W. X. Ji, Y. Q. Lan, *Angew. Chem., Int. Ed.* **2020**, *59*, 2659.
- [14] a) Y. Fu, D. Sun, Y. Chen, R. Huang, Z. Ding, X. Fu, Z. Li, *Angew. Chem., Int. Ed.* **2012**, *51*, 3364; b) M. E. Mahmoud, H. Audi, A. Assoud, T. H. Ghaddar, M. Hmadeh, *J. Am. Chem. Soc.* **2019**, *141*, 7115; c) Z.-H. Yan, M.-H. Du, J. Liu, S. Jin, C. Wang, G.-L. Zhuang, X.-J. Kong, L.-S. Long, L.-S. Zheng, *Nat. Commun.* **2018**, *9*, 3353; d) Y. Lee, S. Kim, J. K. Kang, S. M. Cohen, *Chem. Commun.* **2015**, *51*, 5735.
- [15] a) C. Wang, Z. Xie, K. E. deKrafft, W. Lin, *J. Am. Chem. Soc.* **2011**, *133*, 13445; b) Y. Wang, N. Y. Huang, J. Q. Shen, P. Q. Liao, X. M. Chen, J. P. Zhang, *J. Am. Chem. Soc.* **2018**, *140*, 38; c) H. B. Zhang, J. W. Nai, L. Yu, X. W. Lou, *Joule* **2017**, *1*, 77; d) J. Zhao, Q. Wang, C. Y. Sun, T. T. Zheng, L. K. Yan, M. T. Li, K. Z. Shao, X. L. Wang, Z. M. Su, *J. Mater. Chem.* **2017**, *5*, 12498; e) T. Ouyang, H. H. Huang, J. W. Wang, D. C. Zhong, T. B. Lu, *Angew. Chem., Int. Ed.* **2017**, *56*, 738; f) W. Liu, X. Li, C. Wang, H. Pan, W. Liu, K. Wang, Q. Zeng, R. Wang, J. Jiang, *J. Am. Chem. Soc.* **2019**, *141*, 17431; g) X. Chen, Q. Dang, R. Sa, L. Li, L. Li, J. Bi, Z. Zhang, J. Long, Y. Yu, Z. Zou, *Chem. Sci.* **2020**, *11*, 6915; h) X. Liu, S. Inagaki, J. Gong, *Angew. Chem., Int. Ed.* **2016**, *55*, 14924.